Bio-Design and Manufacturing (2026) 9:137–152
https://doi.org/10.1631/bdm.2500179

RESEARCH ARTICLE

Effect of surface area and pore size on long-term bone regeneration: dynamic changes in geometric characteristics, mass transport, and mechanobiology

Xing Peng[1] · Guoxian Zhang[1,2] · Jian Pu[1] · Shu Yang[3] · Wen Cui[4] · Xue Zhou[5] · Shuxin Qu[6] · Zhongmin Jin[1,7]

Received: 10 April 2025 / Accepted: 12 July 2025

Abstract

The specific surface area (S_S) and pore size (D) exhibit an inherent trade-off in the microscale design of bone implants: larger pores typically correlate with reduced surface area and vice versa. This relationship has attracted notable attention because of its critical role in the regulation of cell adhesion and osteogenesis. However, it remains largely unclear how S_S and D affect the generated bone tissue and dynamically change during long-term osteogenesis. Herein, by applying rigorous geometric mapping to minimal surfaces, we constructed precisely partitioned and layer-by-layer thickened tissue models to simulate osteogenesis across different temporal scales and thereby track the dynamic evolution of geometric characteristics, permeability, and mechanobiological tissue differentiation. The high-S_S samples were found to facilitate the rapid formation of new bone tissue in the early stages. However, their smaller pores tended to cause occlusions, hindering further tissue development. In contrast, low-S_S samples showed slower bone regeneration, but their larger pores provided adequate physical space for tissue regeneration and mass transport, ultimately promoting bone formation in the long term. Mechanobiological regulation suggests that fibrous tissue formation inhibits additional bone formation, establishing a dynamic equilibrium between osteogenesis and pore space to sustain nutrient/waste exchange throughout the regenerative process. Overall, smaller pores are preferable in implants for minimally loaded osteoplasty procedures focused on early-stage bone consolidation, whereas larger pores are preferable in dynamically loaded implants requiring prolonged mechanical stability.

✉ Jian Pu
pu1995@my.swjtu.edu.cn

✉ Zhongmin Jin
zmjin@swjtu.edu.cn

[1] Tribology Research Institute, School of Mechanical Engineering, Southwest Jiaotong University, Chengdu 610031, China

[2] School of Mechanical Engineering, Xihua University, Chengdu 610039, China

[3] Greater Bay Area Center for Medical Device Evaluation and Inspection, NMPA, Shenzhen 518000, China

[4] Beijing AKEC Medical Co., Ltd., Beijing 102200, China

[5] School of Mechanical Engineering, Sichuan University, Chengdu 610065, China

[6] Institute of Biomedical Engineering, College of Medicine, Southwest Jiaotong University, Chengdu 610031, China

[7] School of Mechanical Engineering, University of Leeds, Leeds LS2 9JT, UK

Graphical abstract

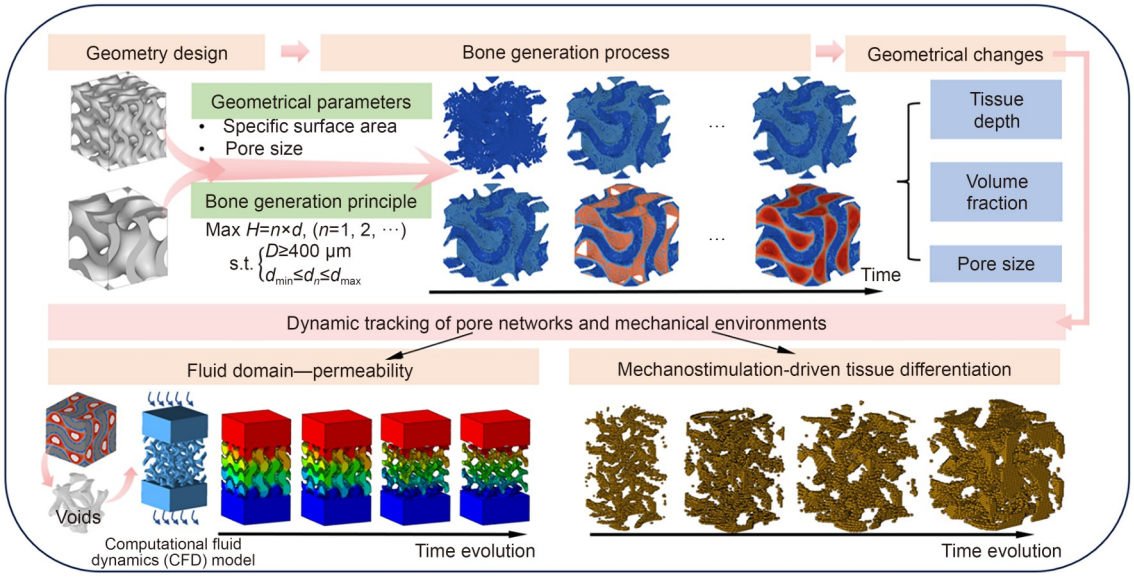

Keywords Minimal surface · Specific surface area · Pore size · Bone ingrowth · Mechanobiology · Finite element simulation

1 Introduction

Porous materials have emerged as a promising paradigm for bone repair implants because their elastic modulus can be tailored to match that of bone tissue through porosity modulation, with the porous structure simultaneously providing physical space for nutrient diffusion and facilitating bone regeneration [1, 2]. In contrast to cemented implants, porous implants foster bone ingrowth at the bone–implant interface, resulting in the stable integration of porous implants with the host bone and superior long-term prosthesis survival rates [3, 4]. However, clinical data indicate that some surgeries still lean toward cemented prostheses [5]. Cementless prostheses require a longer time to achieve osseointegration and are susceptible to periprosthetic fractures during the early postoperative period. Thus, cemented implants are often recommended for elderly patients [6]. In recent years, the rising prevalence of extreme sports and traumatic fractures has led to increased demand for bone implants with enhanced longevity and functional capacity (e.g., enabling high-impact activities such as hiking and running) from younger patients [7, 8]. This shift has driven innovations in porous implant design, targeting accelerated bone ingrowth, robust interfacial bonding, and improved load-bearing capabilities.

Recently, metals, ceramics, and polymers with superior biocompatibility have attracted substantial attention as bone–implant materials [9, 10]. However, given the critical requirement for long-term biocompatibility and mechanical reliability, metallic bone implants remain dominant in both commercial adoption and clinical implementation. Currently, the central research challenge in the field is the optimization of their structural design. At the macroscopic scale, functional-gradient architectures are widely employed to mimic the mechanical gradients of cortical and cancellous bone [11]. These gradients are typically realized through porosity gradients [12, 13], structural-type gradients [14], and unit cell size gradients [15, 16]. Indeed, current investigations preferentially employ micro- and mesoscale architectures (100–1500 μm) to mimic the mechanical and biological characteristics of cancellous bone [17]. Previous studies have extensively explored geometry–property relationships in lattice structures, minimal surface structures, and random biomimetic structures, aiming to meet the requirements of bone implants in terms of key properties such as elastic modulus, yield strength, and permeability [18, 19]. Nevertheless, empirical evidence suggests that structural complexity alone does not inherently enhance functional performance, as mechanical requirements can be satisfied solely by adjusting the porous structure. In contrast, fundamental geometric parameters play a pivotal role in bone regeneration. For example, pore size governs mass transport efficiency [20], whereas surface area determines initial cell attachment and tissue colonization capacity [21]. Evidence suggests a trade-off between pore size and surface area in bone implants: the smaller the pore size of a

material, the larger its specific surface area [22]. Most critically, pore size and surface area dynamically change with bone ingrowth: newly formed bone tissue occupies the pores, thereby reducing the capacity for mass transport [23, 24]. Currently, the optimal balance between pore size and surface area for the long-term service of implants remains unclear.

Notably, in preclinical studies on animal models (e.g., mice, rabbits), construct dimensions rarely exceed 10 mm. Consequently, new bone tissue rapidly fills the entire scaffold within 4–12 weeks [20, 25], suggesting an optimal pore size range of 500–1000 μm. However, in clinical studies, many large-segment bone defects exceed the critical size of 3–5 cm [26]. Bone regeneration originates from the bone–implant interface, and newly formed bone tissue can block the pores, complicating deep bone ingrowth. This phenomenon is exemplified by results obtained for a critical-sized sheep tibial defect model (15 cm): after 24 weeks, substantial bone deposition occurred at the interface, whereas minimal ingrowth was observed in the mid-region of the scaffold [27]. These findings indicate that the 500–1000 μm pore size is effective in small animal models but fails to address the temporal and spatial complexities of osseogenesis in large-segment implants, where prolonged bone ingrowth is hampered by the dynamic constraints imposed on nutrient diffusion efficiency by newly formed bone. Consequently, implant design must reconcile two competing priorities: achieving a sufficient bone generation rate while maintaining long-term mass transport capacity.

To address the above issues, the present study used minimal surface structures and scaling of unit cells to obtain samples with controlled pore sizes and surface areas. By progressively adding precisely partitioned thin layers to the surface of the porous structure, the long-term bone regeneration was simulated, and the hindering effects of newly formed bone tissue on mass transport were investigated. Additionally, a biophysical model was constructed to explore the changes in the biomechanical environment caused by newly formed bone tissue during long-term osseoregeneration.

2 Materials and methods

2.1 Structure design and fabrication

A Gyroid structure was adopted as the foundation; its mathematical equation is shown below:

$$\sin\left(\frac{2\pi}{L}x\right)\cos\left(\frac{2\pi}{L}y\right)+\sin\left(\frac{2\pi}{L}y\right)\cos\left(\frac{2\pi}{L}z\right)+\sin\left(\frac{2\pi}{L}z\right)\cos\left(\frac{2\pi}{L}x\right)=t, \quad (1)$$

where x, y, and z are the coordinates of a point in the design space, and L is the dimension of the Gyroid unit cell in the x, y, and z directions. Parameter t is linearly related to the porosity (P) of the structure [28]. In the present study, all samples had 65% porosity (i.e., $-0.525<t<0.525$), and the unit cell size was varied from 1.5 to 3.0 mm by adjusting parameter L. The Gyroid minimal surface is typically categorized into network and matrix types [29]. Herein, the shell-based matrix samples were designated as M15–M30 (Fig. 1a). These samples were fabricated from photosensitive resin (TAPS 400P, POLLY POLYMER, China) using 405-nm light, followed by a 30-min ultraviolet curing post-processing (Fig. 1b).

The pore size and specific surface area were measured using HyperMesh software (version 2023, Altair Engineering, USA). Pore size, defined as the normal distance between adjacent pore walls (Fig. 1a), is positively correlated with oxygen/nutrient transport capacity [22, 30]. The specific surface area (S_S) represents the space per unit volume available in an implant for cell adhesion and tissue growth:

$$S_S=\frac{S}{L^3}, \quad (2)$$

where S and L are the surface area and dimension of the unit cell, respectively [21]. With an increase in the size of the unit cell, the pore size and specific surface area change in opposite directions (Fig. 1c).

2.2 Simulation of long-term bone generation

Surface area and pore size both play important roles in bone regeneration, yet they are in a trade-off and must be dynamically balanced for long-term bone regeneration. The present study focused on the interplay between geometric characteristics at the bone–implant interface and bone regeneration. Long-term bone regeneration is challenging to predict with precision [31, 32]. Herein, we considered long-term bone regeneration as a stable process wherein bone tissue is generated uniformly over time on the implant surface, leading to cumulative bone formation over time. However, the newly formed bone tissue progressively occludes the pores, thereby impairing mass transport [23]. Considering the pore size and permeability of human bone [22], we hypothesized that bone formation ceases when the pore size (D) decreases below 400 μm. The mathematical description is as follows:

$$\begin{aligned}&\text{Max } H = n \times d,\ n = 1, 2, \cdots\\ &\text{s.t. } \begin{cases} D\geq 400\ \mu\text{m}, \\ d_{\min}\leq d_n\leq d_{\max}, \end{cases}\end{aligned} \quad (3)$$

where d is the thickness of bone tissue generated per unit time, n denotes different time phases, and H is the total bone thickness. Here, $d_{\min}$ and $d_{\max}$ represent the spatial

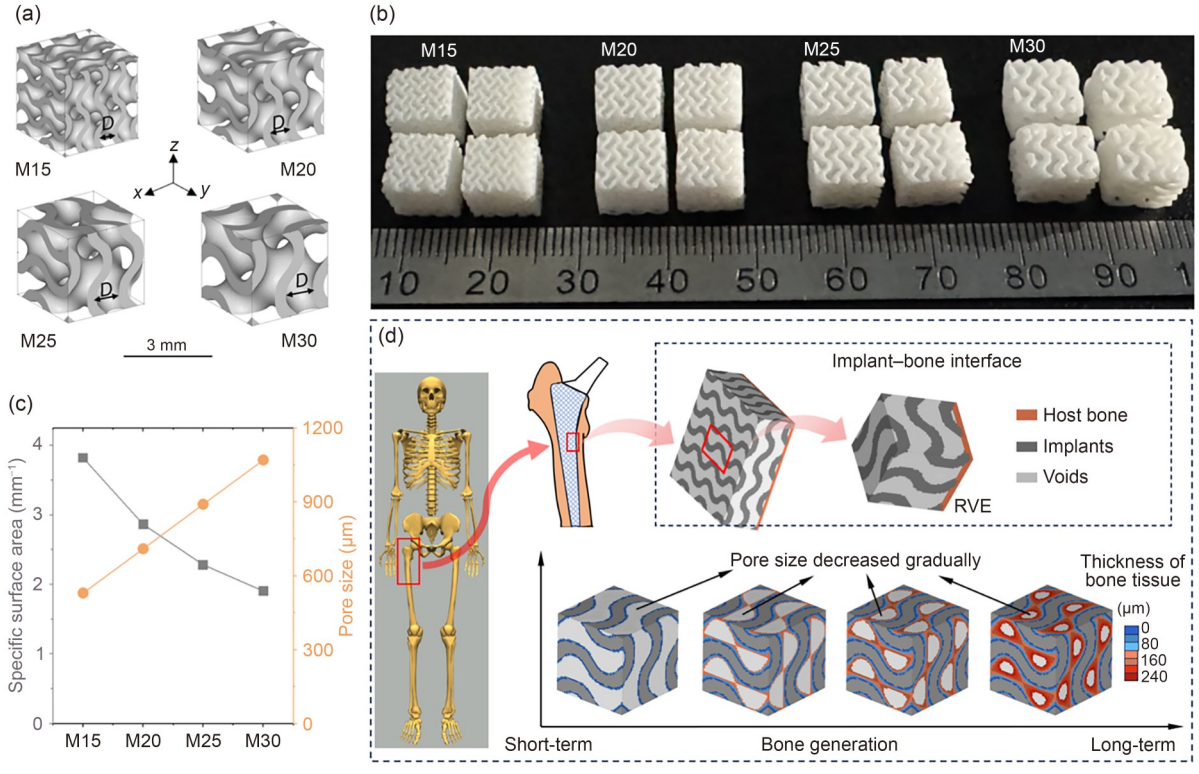

Fig. 1 Design of porous structures and modeling of bone regeneration volume. Designed (a) and fabricated (b) samples with 1.5–3.0 mm unit cell size, named M15–M30, respectively. (c) Specific surface area and pore size exhibit opposite trends with increasing unit cell size. (d) At the bone–implant interface, newly formed bone tissue progressively thickens and replaces the voids over time, during which the pore size gradually decreases. The color gradient from blue to red indicates the increase in the thickness of bone tissue. RVE: representative volume element

constraints provided by the porous structure, meaning that new tissue can only grow within the pores. As bone tissue can only grow between the implant walls, its spatial distribution is constrained by d_n. Through this approach, we substituted temporal effects with the spatial distribution of bone regeneration (Fig. 1d). Wall thickness (l_w) of the Gyroid structure can be described as [33]

$$l_w = \frac{(1-P)\times L^3}{S_0}, \tag{4}$$

where S_0 is the surface area of the unit cell at t=0, and L and P are the dimensions of the unit cell and porosity, respectively. In the present study, all the samples had 65% porosity; thus, the relationship between bone thickness (H) and porosity (P) can be expressed as follows:

$$P = 0.65 - \frac{HS_0}{L^3}. \tag{5}$$

Given that $H=n\times d$ (n=1, 2, ⋯), we used d=40 μm to determine the corresponding porosity for each H, followed by spatial modeling (Fig. 1d). Equation (5) describes the relationship between initial porosity and bone tissue thickness. However, with increasing thickness of the bone tissue, the specific surface area (S_0) available for bone regeneration changes, rendering this linear relationship inapplicable. For this reason, we first adjusted structural porosity to derive the corresponding bone regeneration thickness, thereby establishing the porosity–tissue thickness relationship. Through parameter modulation, the uniform thickening of bone tissue was achieved.

2.3 Geometric characteristics

In architecturally complex scaffolds, staged 40 μm augmentations in the orthogonal dimension constrain pore size while modulating bone volume fractions. Through precise geometric segmentation, we dynamically tracked parameter shifts across different time spans, investigating the impact of size scaling parameters on bone regeneration at the bone–implant interface (Fig. 2a).

2.4 Mechanical and mass transport properties

Given that elastic compatibility with the host bone is a fundamental requirement for porous implants [34], the mechanical properties of the fabricated scaffolds were characterized. Uniaxial compression tests (E10000, Instron, USA) were performed following the ISO 13314 standard at a displacement rate of 0.5 mm/min [35]. The elastic modulus (E)

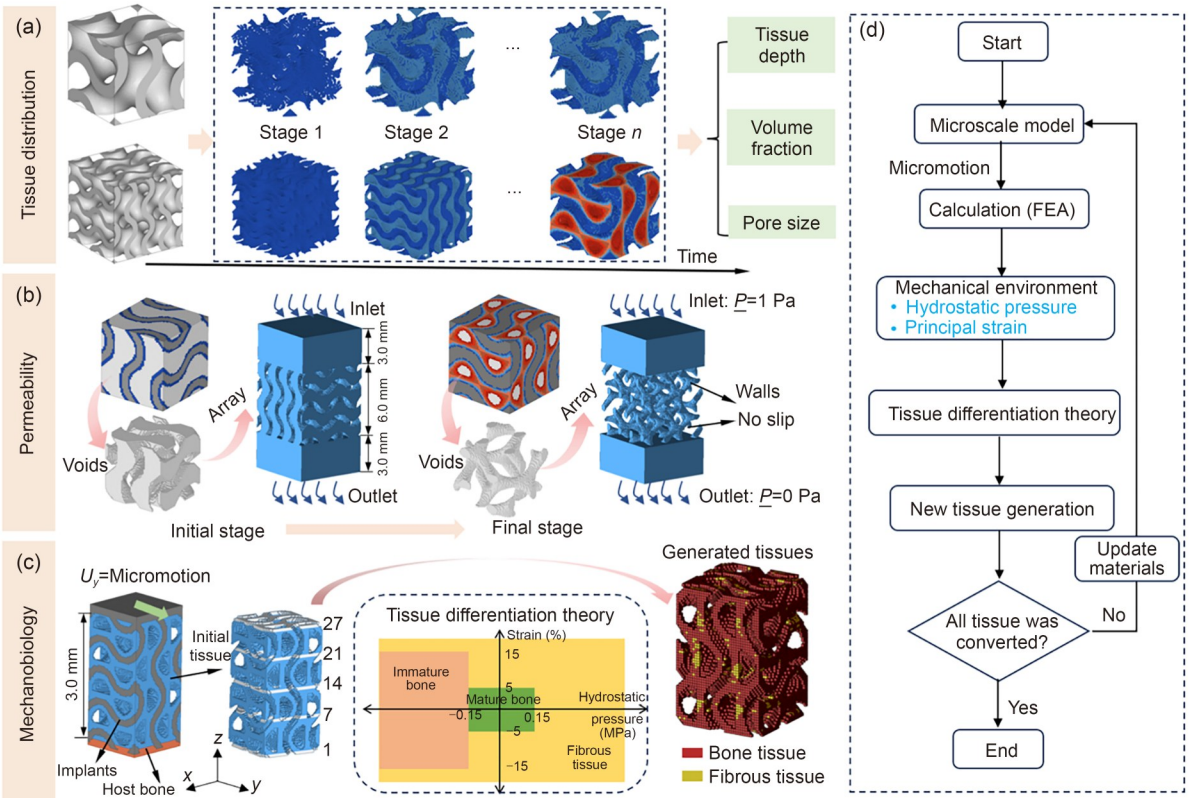

Fig. 2 Geometric feature modeling, permeability assessment, and tissue regeneration calculation process. (a) Volumetric partitioning of bone regeneration from short-term to long-term stages. In each stage, the bone tissue was thickened in 40 μm increments along the normal direction until the pore size was reduced below 400 μm. The color bar indicating bone tissue thickness is the same as in Fig. 1d. (b) CFD models for calculating permeability at different bone regeneration stages. (c) The finite element model for simulating tissue differentiation under mechanical stimulation. The granulation tissue undergoes transformation into bone tissue or fibrous tissue based on the local hydrostatic pressure and principal strain derived from the tissue differentiation theory. (d) The framework for simulating tissue differentiation. FEA: finite element analysis

was calculated as the linear-regression slope of the stress–strain curve, with yield stress (σ) defined at 0.2% plastic strain. As the present study primarily investigated the effects of structural scaling on the scaffold modulus, all test results were normalized; i.e., $\underline{E}=E/E_m$, $\underline{\sigma}=\sigma/\sigma_m$, where $\underline{E}$ and $\underline{\sigma}$ are the normalized forms of elastic modulus and yield stress, respectively. E_m and σ_m are the corresponding parameters of the matrix material, 1080.5 MPa and 45.3 MPa, respectively, which were determined through the compressive test of dense samples (see Fig. 3a for details). It should be emphasized that elastic modulus matching is the primary requirement for bone implants. Therefore, we investigated how unit cell scaling affects the elastic modulus while employing normalization methods to conclusively prove that these effects originate from structural characteristics rather than material properties.

Considering mass transport characteristics, newly formed bone tissue progressively occludes the pore network, leading to a continuous reduction in the available capacity of mass transfer pathways over time. We established computational fluid dynamics (CFD) models (Abaqus 2016/CFD solver) for each stage, from short-term to long-term, to quantify the dynamic evolution of permeability. The geometric models for fluid computations were constructed by performing Boolean operations with solids (implants and bone tissues, Fig. 2b), with the employed fluid being water with a dynamic viscosity (μ) of 0.001 Pa·s and a density of 1000 kg/m^3 [36]. To avoid the boundary effect caused by the inlet and outlet areas, virtual fluid domains were defined on both sides. A boundary condition for permeability simulation with a pressure of 1 Pa at the inlet and 0 Pa at the outlet was applied [22]. The permeability (K) was calculated as

$$K=\frac{v\mu L_f}{\Delta P}, \tag{6}$$

where v is the fluid velocity obtained through CFD results, L_f is the length of the fluid domain (6.0 mm, Fig. 2b), and ΔP is the pressure drop between the inlet and outlet.

Referring to previous studies [22, 37], a hexahedral voxel mesh was used in both the mechanical and CFD models, and a mesh size of $L/27$ was adopted based on the results of the sensitivity analysis.

2.5 Mechanoregulatory tissue differentiation

Although many studies [2, 38] have focused on the mechanical properties of the porous implants, their interactions with the generated tissue require further investigation. Because of the immense computational cost, complete bone regeneration calculations are difficult to perform at the joint scale. Thus, these calculations are usually conducted locally using a representative volume element (RVE). Figure 2c shows the RVE from the bone–implant interface, which consists of a porous structure, host bone, and granulation tissue. Over time, the bone tissue progressively thickened. We conducted precise modeling of the granulation tissue at each temporal stage and investigated the mechanical micro-environment governing its differentiation.

According to a previous study on total hip arthroplasty [39], the micromotion range of 60–150 μm was adopted as the boundary condition. In these finite element models, the bottom of the RVE was fixed, and periodic boundary conditions were applied to the side surfaces of the RVE. The material properties of RVE (Table 1) were obtained from the literature [40–42]. The simulations were performed using Abaqus, and the data were transferred via Python.

Table 1 Input material properties used in tissue differentiation models

Component	Elastic modulus (MPa)	Poisson ratio
Granulation tissue	1	0.167
Porous implant (Ta)	31 510	0.34
Host bone	1700	0.3
Fibrous tissue	2	0.167
Immature bone	1000	0.3
Mature bone	6000	0.3

The computational process of tissue differentiation is presented in Fig. 2d. In the initial stage, the granulation tissue was divided into 27 layers (Fig. 2c). For each layer, the transitional layer between the previously formed bone tissue and granulation tissue was transformed into bone tissue and fibrous tissue (Fig. 2c) depending on the hydrostatic pressure (p) and principal strain (ε) [43]. Specifically, the following tissue differentiation rules were employed:

$$\begin{cases} \text{Mature bone} & \text{if} \quad \Omega_1 \in \left(0.15 > p > -0.15, 0.05 > \varepsilon > -0.05\right), \\ \text{Immature bone} & \text{if} \quad \Omega_2 \in \left(0.15 > p, 0.15 > \varepsilon > -0.15\right), \\ \text{Fibrous tissue} & \text{if} \quad \Omega_3 = \Omega - \Omega_1 - \Omega_2, \end{cases} \tag{7}$$

where Ω is the entire region with p and ε, and Ω_1, Ω_2, and Ω_3 are the p and ε regions corresponding to mature bone, immature bone, and fibrous tissue, respectively. The mesh type and size of tissue differentiation simulation were the same as those provided in Sect. 2.4.

3 Results and discussion

3.1 Mechanical properties of scaffolds

Figure 3a shows the force–displacement curve of the dense compressive sample, from which the elastic modulus (1080.5 MPa) and yield stress (45.3 MPa) of the matrix material were obtained. The mass of the scaffolds was obtained through weighing (Fig. 3b) and further used to calculate the actual porosity of the samples. With the designed value of 65%, the actual porosity ranged from 64.43% to 70.28%. The force–displacement curves of the four porous scaffolds are shown in Fig. 3c. From M15 to M30, the normalized elastic modulus (Fig. 3d) decreases from 0.068 to 0.054, and the yield stress (Fig. 3e) declines from 0.078 to 0.055, with discrepancies of 20.17% and 29.73%, respectively.

Although the elastic modulus of the scaffold is theoretically determined by porosity, manufacturing deviations induced by unit cell scaling can lead to discrepancies [30]. Consistent with our findings, previous studies reported that an increase in the unit cell size of pure titanium scaffolds from 3 to 5 mm results in a decrease of 25.5% in the elastic modulus [44]. Additive manufacturing principles suggest that smaller unit cells exhibit more abrupt geometric transitions, which tend to promote material adhesion [45, 46]. This results in a greater effective load-bearing volume and consequently higher elastic modulus. It should be noted that the elastic moduli of the implant and host bone are considered matching if the value for the implant falls within a specific range, 13–30 GPa for cortical bone and 0.1–1.0 GPa for cancellous bone [47]. Consequently, the variation in elastic modulus induced by unit cell scaling in the present study falls within acceptable clinical tolerances and would not compromise elastic compatibility. This allows the comparison of the biological performance characteristics of the implants.

3.2 Geometric characteristics at different stages

Over time, the bone tissue on the structural surface gradually thickens, with larger unit cell (pore) sizes allowing prolonged bone regeneration (Fig. 4a). For instance, bone regeneration ceases by stage 3 on M15 (pore size <400 μm) but continues to stage 9 on M30 (Fig. 4b). At the same time, the bone growth rate increases with the specific surface area of the implants. By stage 3, the volume fraction of bone tissue is 34.7% in the M15 group and just 24.9% in the M30 group. However, the M30 group shows greater sustainable growth potential, ultimately achieving 51.1% volume fraction, significantly higher than that of M15 (Fig. 4c).

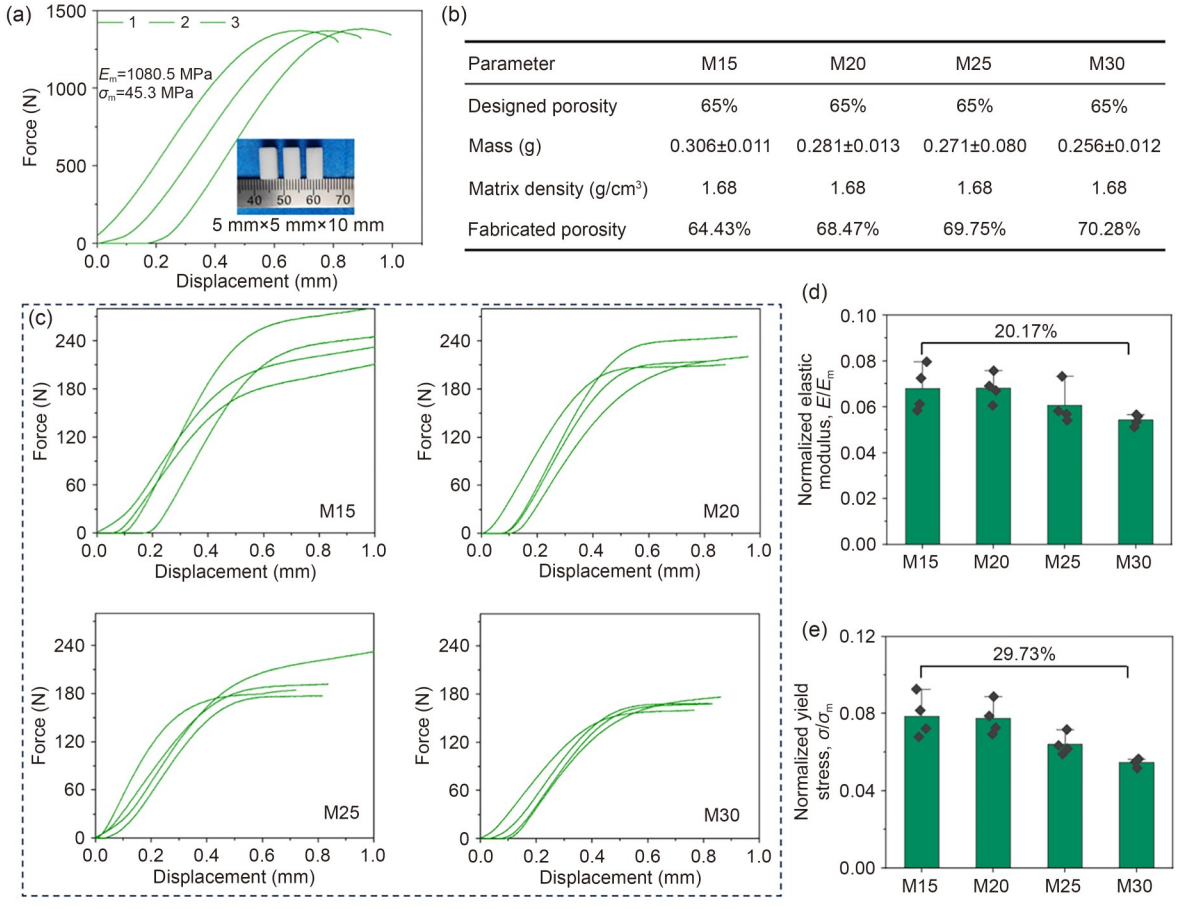

Parameter	M15	M20	M25	M30
Designed porosity	65%	65%	65%	65%
Mass (g)	0.306±0.011	0.281±0.013	0.271±0.080	0.256±0.012
Matrix density (g/cm^3)	1.68	1.68	1.68	1.68
Fabricated porosity	64.43%	68.47%	69.75%	70.28%

Fig. 3 Mechanical properties testing of samples. (a) Force–displacement curves for the dense compressive samples. (b) Mass and porosity of the designed and fabricated porous scaffolds. (c) Force–displacement curves for the four samples. Normalized elastic modulus (d) and normalized yield stress values (e) of the porous samples. Data are expressed as mean±standard deviation (n=4)

The computational results indicate the same trend as previous animal experiments [25]. In animal experiments [25], the bone volume to total volume ratio (BV/TV) value of M15 was 64.4% higher than that of M25 at 4 weeks and by 41.7% at 8 weeks. Herein, in stage 1, the BV/TV value of M15 exceeds that of M30 by 58.0% and by 45.3% in stage 2 (Fig. 5).

Theoretically, a larger specific surface area promotes faster bone tissue growth [21]. In rabbit models at 8 weeks, scaffolds with a 1.5 mm unit cell size showed 41.7% greater bone volume than those with 2.5 mm unit cells [25]. The commonly observed time points [15, 17] in animal experiments (4–12 weeks) represent only short-term outcomes, corresponding to stages 1–3 in the present study. This aligns with our finding that the M15 group (small pore size/high surface area) showed higher bone volume than M30 at these early stages. However, this does not validate the suitability of small-pore-size/high-surface-area implants for the regeneration of large-segmental bone defects or joint replacement. In large-segment implants, newly formed tissues rapidly occupy the bone–implant interface, impeding subsequent nutrient transport and deep bone ingrowth [27]. In fact, conventional animal experiments typically employ scaffolds with diameters less than 10 mm, on which this critical phenomenon is difficult to observe. Therefore, our findings indicate that although bone generation is slower in large pore implants due to their limited surface area, their structural architecture provides essential physical conditions for sustained, deep bone ingrowth.

3.3 Permeability at different stages

Figure 6a shows the local pressure and flow velocity from the representative CFD model, with velocity distributions visualized through cross-sectional views. Figure 6b presents the time-dependent CFD models of M30, indicating that the fluid domain space (pore size) progressively diminishes over time. An identical pressure drop (1 Pa) was maintained in all models, allowing the direct visualization of their permeability through flow velocity profiles. The maximum flow velocity reaches 8 mm/s in M30 and only 4 mm/s in M15. Because of changes in pore size, flow velocity in M15 approaches its minimum value by stage 4, whereas in

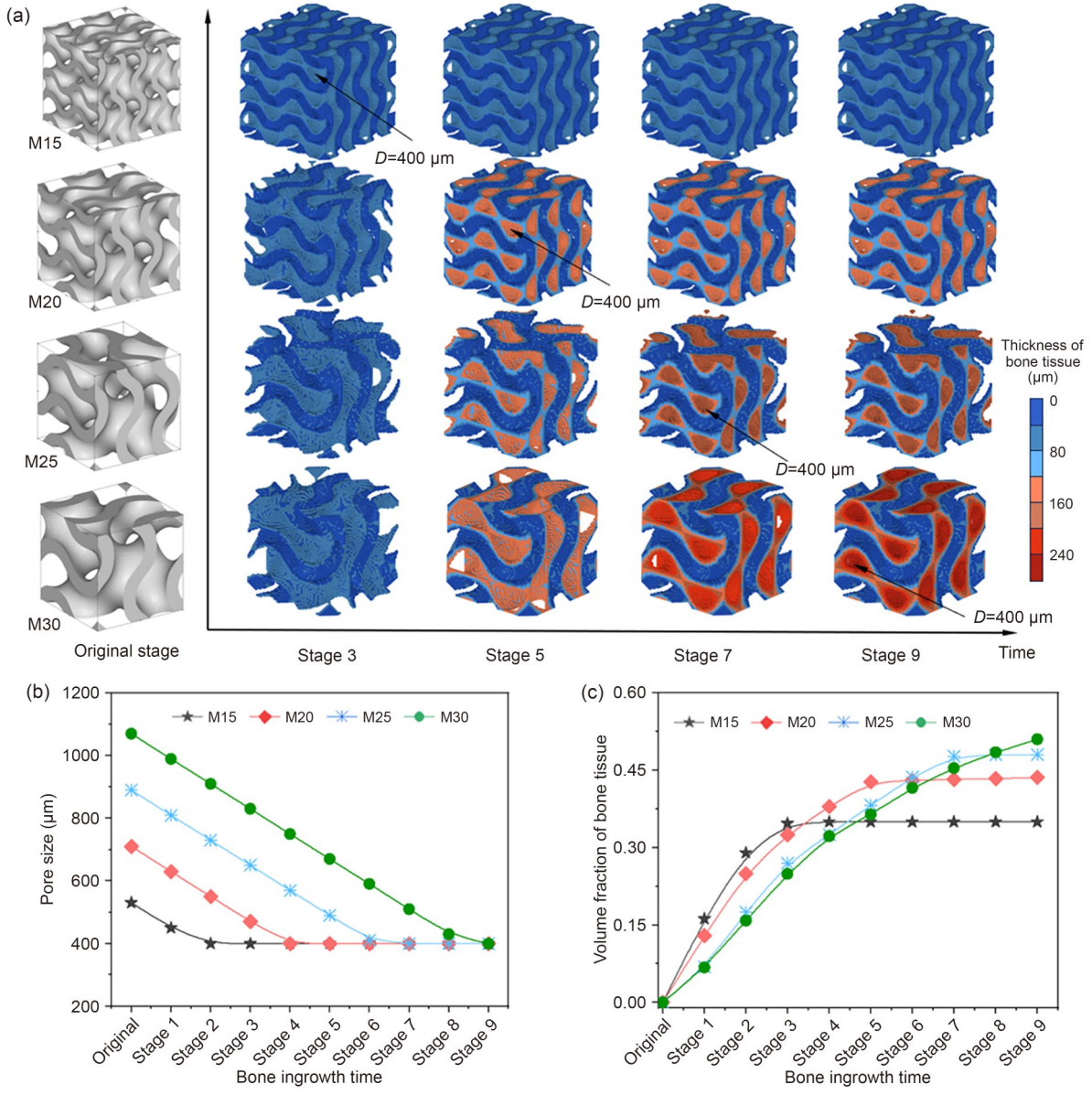

Fig. 4 Evolution of geometric features during the bone regeneration process. (a) Precise spatial distribution of generated bone volume in the four sample groups at different stages. Changes in pore diameter (b) and volume fraction (c) of generated bone tissue

M30, fluid flow is maintained until the final stage (Fig. 6c). The permeability corresponding to flow velocity also differs among the samples: M15 shows lower initial permeability (2.42×10^{-9} m^2) that rapidly decreases below the minimum threshold, whereas M30 exhibits higher initial permeability (8.13×10^{-9} m^2) that gradually decreases until the final stage (Fig. 6d). At a pore size of 400 μm, all structures show similar permeability (0.26×10^{-9}–0.44×10^{-9} m^2), consistent with the lower permeability limit of natural human bone tissue (0.2×10^{-9}–0.5×10^{-9} m^2 [48, 49]). This finding confirms the 400 μm pore size constraint employed herein.

Permeability, which reflects the transport capacity of nutrients and metabolic waste, is positively correlated with pore size (D) and negatively correlated with specific surface area (S_S). This relationship can be expressed by the Kozeny equation [50]:

$$K = \frac{1}{C_K}\left(\frac{D^3}{S_S}\right), \tag{8}$$

where C_K is a constant determined by the microstructure. In terms of spatial distribution, pores and the solid matrix are interlocked with each other. Consequently, the material transport capacity (governed by porosity) competes with the mechanical properties (determined by the solid material) [1, 22]. Previous studies have attempted to decouple these properties or simultaneously enhance both by tailoring the microstructure [21, 51]. However, these investigations focused

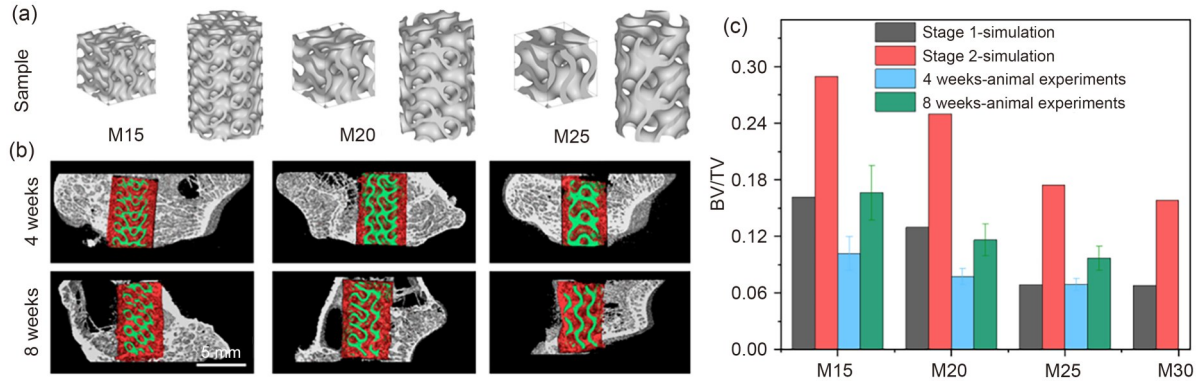

Fig. 5 Comparison of experimental and computational results in bone regeneration. (a) Cylindrical scaffolds used in animal experiments and corresponding unit cell models. (b) Bone regeneration results for M15–M25 scaffolds in animal experiments (reproduced from [25], licensed under CC BY 4.0). (c) Comparative validation between simulation results of the present study and previous reports on bone formation in animals. Data are expressed as mean±standard deviation (n=6)

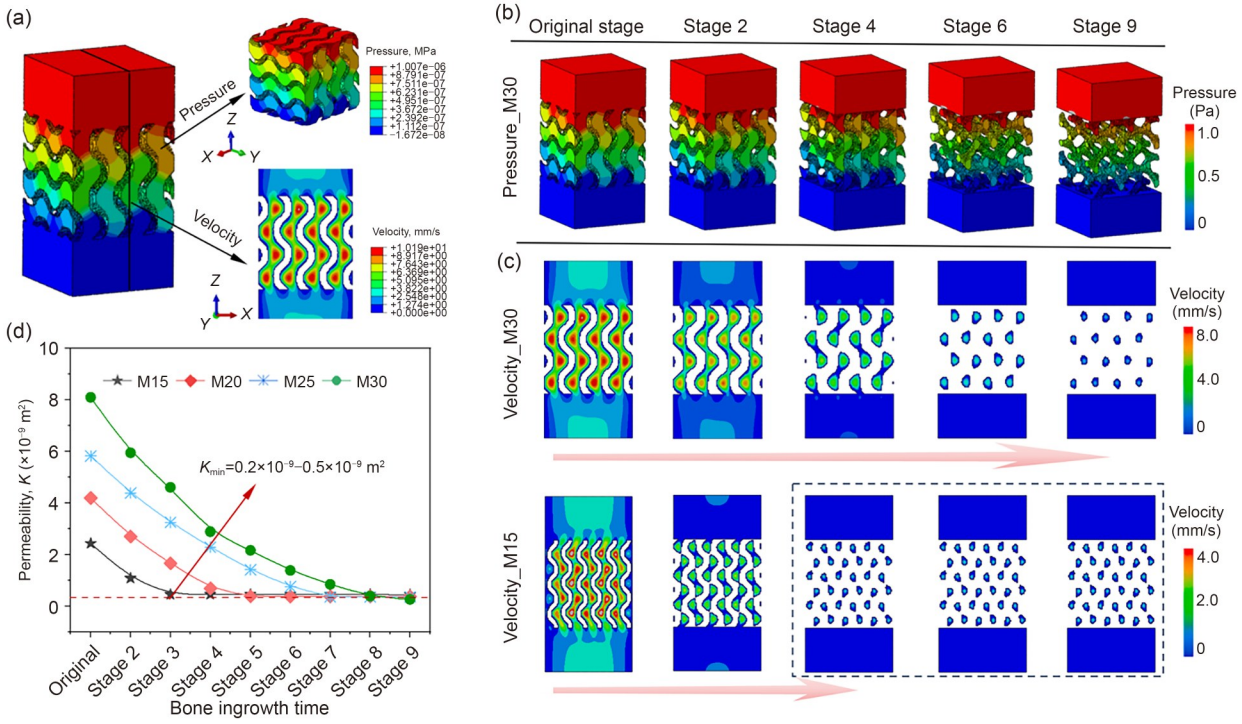

Fig. 6 Dynamic changes in permeability during bone regeneration. (a) Representative CFD model for pressure and fluid velocity. (b) CFD models for sample M30 at different stages. The same boundary conditions (inlet: 1 Pa; outlet: 0 Pa) were applied to all models. (c) Changes in fluid velocity across different stages. (d) The permeability of samples. All the samples exhibit similar minimum permeability, consistent with the lower permeability limit of natural human bone tissue (0.2×10^{-9}–0.5×10^{-9} m^2)

solely on the initial state of scaffolds and did not assess long-term bone regeneration. Our findings reveal that during prolonged bone regeneration, small pores at the bone–implant interface are rapidly occluded, hindering bone ingrowth into the implant.

3.4 Mechanoregulatory tissue differentiation

Figure 7a shows the complete tissue differentiation in a representative RVE. Within a single stage, granulation tissue progressively grows from the proximal end of the host bone and gradually differentiates into bone tissue (mature bone and immature bone) and fibrous tissue (Fig. 7a). The thickness of the newly formed tissue progressively increases throughout the stages. Notably, the fibrous tissue, which cannot be reinforced or resorbed, impedes the growth of bone tissue [43]. First, we examined tissue differentiation at identical growth durations (stage 3). The distribution of fibrous tissue in samples under different micromotion conditions is shown in Fig. 7b. In stage 3, the proportion of

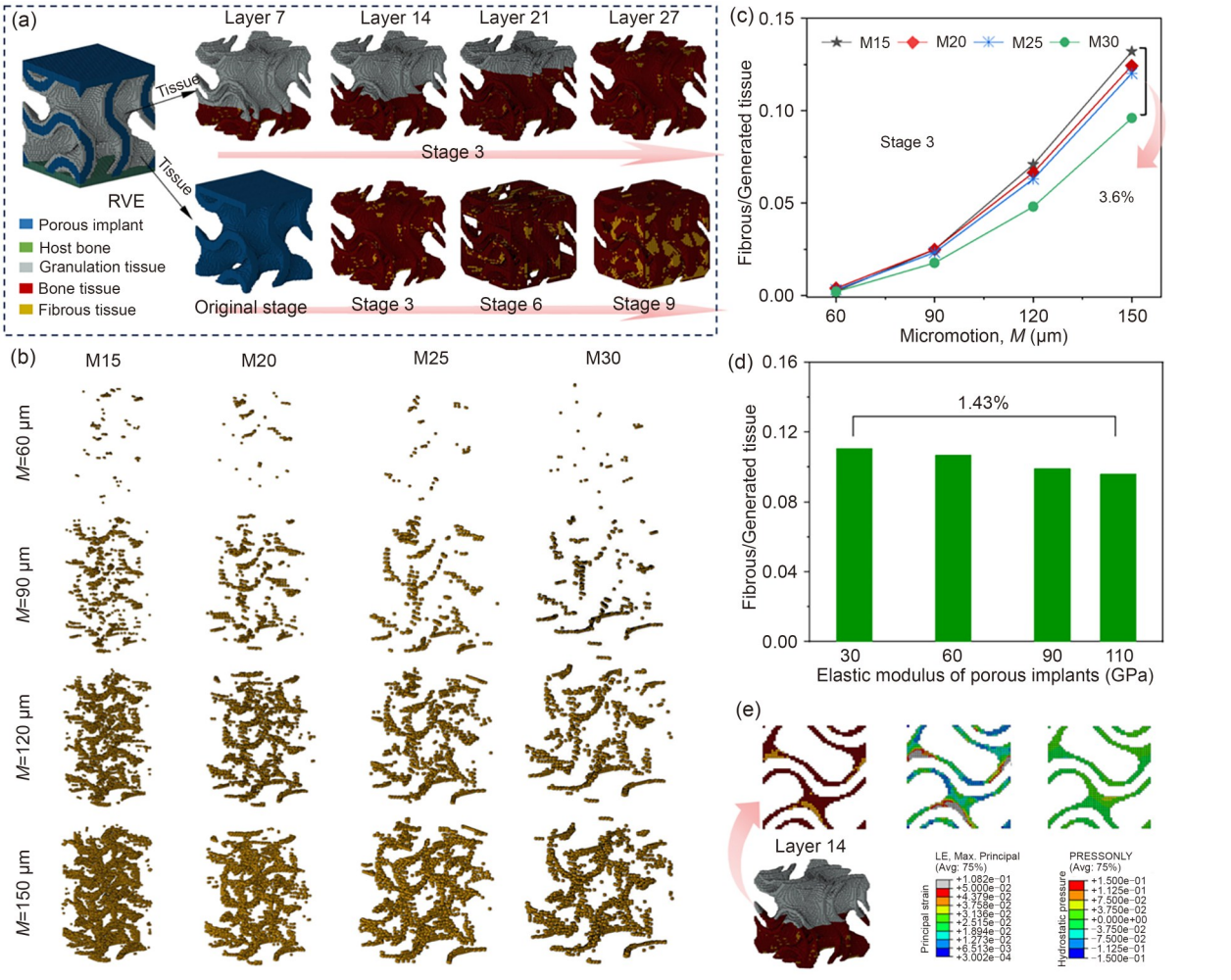

Fig. 7 Effect of pore diameter/surface area on the mechanical environment of tissue differentiation. (a) Complete tissue differentiation within a representative RVE. The fibrous tissue (b) and statistical data of samples (c) under different micromotions. The values for fibrous/generated tissue show a maximum variation of 5% among the samples. (d) The effect of the matrix elastic modulus on tissue differentiation. (e) Dependence of tissue differentiation on principal strain and hydrostatic pressure

fibrous tissue gradually increases from M15 to M30, with differences consistently maintained within 3.6% (Fig. 7c). This suggests that during the initial post-implantation period, the variation in mechanical stimuli caused by differences in pore size is relatively limited.

Considering that the matrix elastic modulus of bone implants can be selectively adjusted (e.g., polyether ether ketone (PEEK), titanium alloys, and tantalum [52]), the sensitivity of tissue differentiation to elastic modulus was investigated by varying the elastic modulus of M30 specimens within 30–110 GPa. The results indicate that under 150 μm micromotion, the proportion of the fibrous tissue varies by merely 1.43% in specimens with different elastic moduli (Fig. 7d). Based on this, we concluded that within our study model, the elastic modulus of the material negligibly affects tissue regeneration. Even at the maximum modulus of 110 GPa, fibrous tissue is formed in high-strain regions (>0.05), whereas the maximum hydrostatic pressure is far below the 0.15 MPa threshold required for the formation of fibrous tissue. This finding aligns with the results of previous studies, which suggest that bone regeneration is primarily strain-driven [53–55], supporting the mechanical homeostasis theory that bone resorption and reinforcement are governed by strain-dependent rules [56, 57].

Figure 8a presents differences in tissue differentiation over the entire growth cycle. As growth progresses (tissue thickening), the mechanical environment within the scaffold leads to an increase in the proportion of fibrous tissue. Specifically, the fibrous content in newly formed tissue in later stages is higher than that in the early stages. Figure 8b shows tissue distribution across four types of scaffolds at the final stage (stage 9). Under the condition of 150 μm micromotion, the proportion of fibrous tissue in M30 is considerably higher than that in M15 (0.131 vs. 0.263). Moreover, as the volume of newly formed tissue in M30 greatly exceeds that in M15 (Fig. 4c), this implies that the absolute

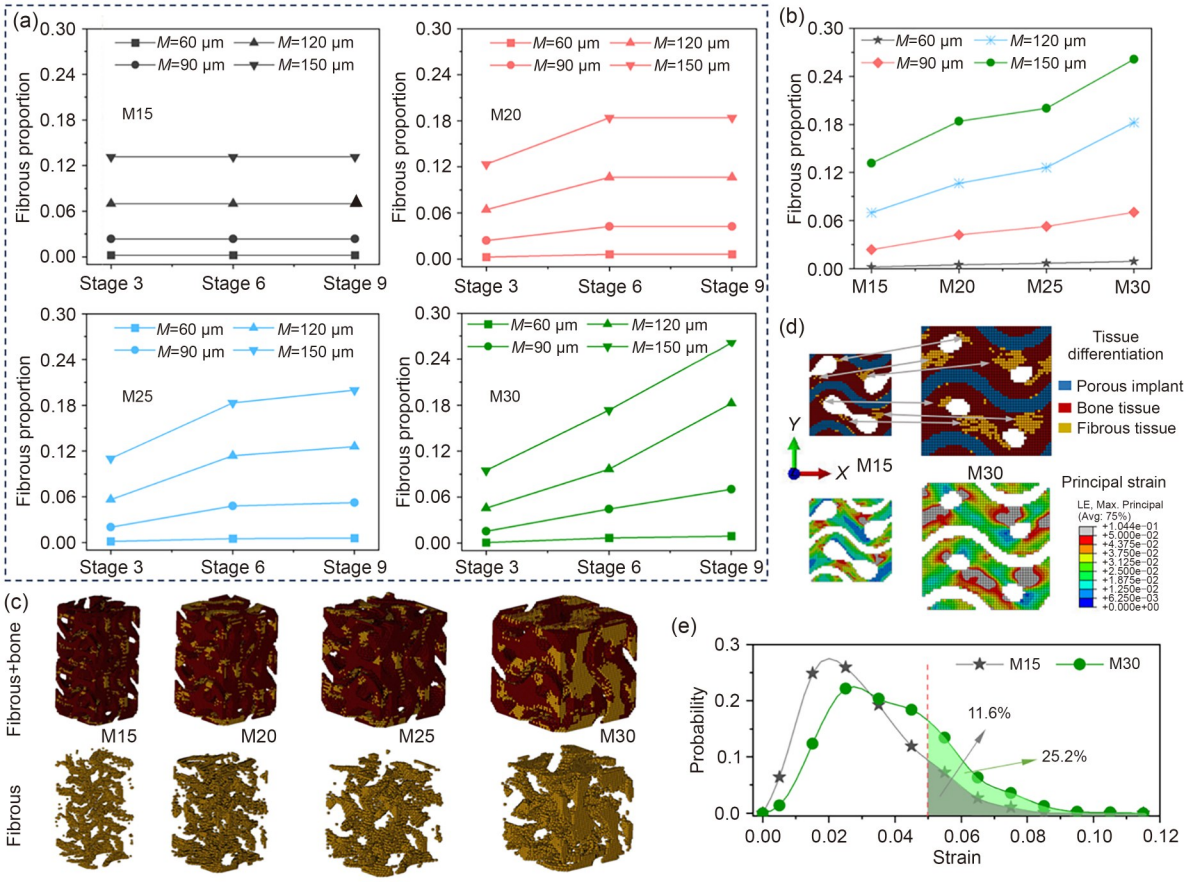

Fig. 8 Tissue differentiation on a temporal scale. (a) Tissue differentiation in samples over the entire growth cycle. (b) Statistical data of tissue distribution across four types of scaffolds at the final stage. (c) Tissue distribution in samples at 150 μm micromotion (stage 9). (d) Localized tissue differentiation and strain distribution in M15 and M30, illustrating the mechanism through which geometric factors affect tissue differentiation. (e) Comparative analysis of strain distribution in M15 and M30 samples

volume of fibrous tissue is greater in M30 than in M15. The detailed spatial distribution of fibrous tissue is shown in Fig. 8c.

Figure 8d shows tissue distribution in cross-sections of identical geometry for the M15 and M30 scaffolds. The results reveal nearly identical spatial distribution patterns of fibrous tissue between the two groups, with the key distinction being that M15 exhibits only sparse fibrous regions, whereas M30 shows notable fibrous aggregation (Fig. 8d). Quantitative measurements of these high-strain regions in the cross-sections (Fig. 8e) show that high-strain regions occupy only 11.6% of the cross-section in M15 and 25.2% in M30. This reveals that fibrous tissue formation in both scaffolds is primarily driven by high-strain regions with similar distribution patterns, whereas the concentrated distribution of newly formed tissue further promotes the aggregation of these high-strain regions.

Figure 9a shows the RVE and the transitional layer between the newly formed tissue and granulation tissue during tissue differentiation in M15 and M30 samples. Figure 9b presents all newly formed tissues in the samples after differentiation. The results indicate that samples with large pore size (M30) consistently exhibit clustered emergence of fibrous tissue formation in both transverse and longitudinal cross-sections, with a substantially higher proportion of fibrous tissue compared to samples with small pore size (M15). The above phenomenon is consistent with the results of previous animal experiments [58]. In samples with pore sizes of 300–900 μm (Fig. 9c), histological staining at 4 weeks (Fig. 9d) reveals that composite regions of fibrous tissue and bone tissue aggregated in areas distant from the host bone (blue area). Woven bone and cartilage near the host bone gradually transitioned into mature bone tissue, while the remaining blue-stained areas primarily represent potential fibrous tissue regions. Notably, samples with P900 exhibit a higher proportion of potential fibrous tissue than samples with P300, and this tissue is present in aggregates in the former samples. Histological sections at 8 weeks reveal reduced impact of bone–implant interface micromotion on regions farther from the host bone (3–6 mm), with fibrous tissue content being lower in these regions. However, P900 samples still exhibit more extensive

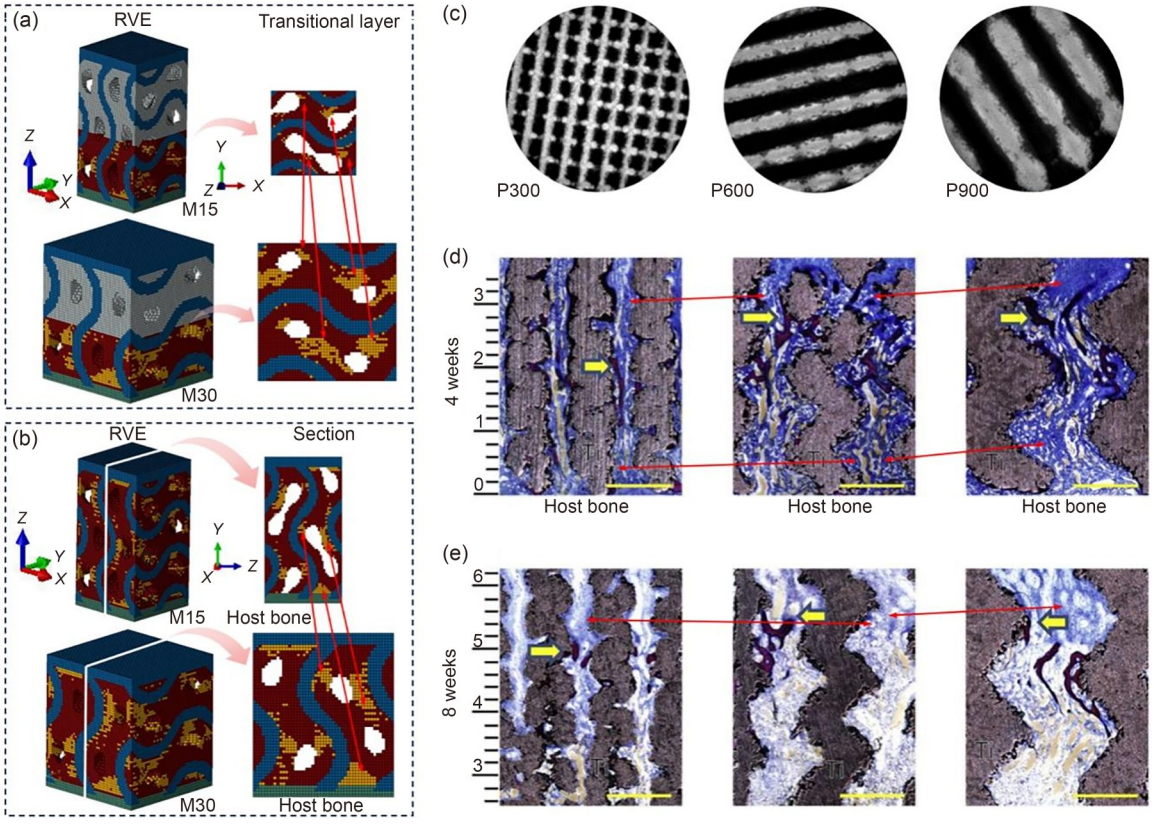

Fig. 9 Comparison of tissue differentiation between the simulation and experiment. (a) Transitional layer between newly formed tissue and granulation tissue in simulated tissue differentiation. (b) Newly formed tissues in samples after differentiation simulation. (c) The geometry section of samples with 300–900 μm pore size in animal experiments (reproduced from [58], with permission from Elsevier B.V.). Non-decalcified histologic sections of cylindrical porous titanium implants implanted into rabbit tibia at 4 (d) and 8 (e) weeks. The reference for the scale cited at the left-hand edge of each image is the distance between the porous structure and the host bone. Staining: Stevenel's blue and Van Gieson's picrofuchsin. Yellow arrow: generated tissue; Red arrow: potential area with emerging fibrous tissue aggregation; Purple: bone tissue; Blue: fibrous tissue and immature bone tissue

and clustered blue-stained regions (fibrous tissue) than P300 samples (Fig. 9e).

In summary, during the early stages of bone regeneration, the variations in mechanical stimulation induced by unit cell scaling were relatively minor. Thus, bone regeneration was predominantly influenced by specific surface area effects in these stages. For instance, a greater volume of bone tissue was generated on the high surface area sample (M15) in the early stages, which is consistent with the results of previous animal experiments at 4–12 weeks [25, 59]. However, over longer periods, bone regeneration was affected not only by reduced permeability but also by the evolving biomechanical environment, which progressively favored the formation of fibrous tissue. This transition ultimately suppressed bone tissue growth.

It is well-known that human bone tissue adapts to its environment through remodeling in response to mechanical stimuli [60, 61]. Although this process has been traditionally simulated at the macroscopic scale, with cancellous bone typically modeled as a dense solid with low modulus, such approaches fail to elucidate how microscopic-scale mechanical stimuli regulate bone regeneration and resorption [62, 63]. Our findings indicate that with the thickening of new bone tissue on trabecular surfaces (or trabecular-like implant surfaces), the resulting biomechanical environment increasingly promotes the differentiation of bone tissue into non-resorbable fibrous tissue. This fibrous tissue effectively inhibits further thickening, thereby maintaining a state of mechanical equilibrium while simultaneously preserving physical space for mass transport.

It is worth noting that the findings of the present study are applicable only to non-degradable materials. The design of biodegradable implants is more complex, as the degradation of their matrix materials must be synchronized with tissue growth [64–66]. Regarding structural factors, specific surface area (S_S) is the most critical factor governing the degradation of metallic scaffolds. Porous scaffolds exhibit considerably higher corrosion rates than bulk metals because of their increased contact area with corrosive media [67]. This implies that the degradation rate of materials with excessively rapid degradation (Mg-based and Zn-based [68, 69]) can be moderated by enlarging unit cell dimensions to

reduce surface area, while thickened pore walls can maintain the mechanical stability of the scaffold over an extended period. For materials with lower degradation rates (Fe-based [70]), the reduction of unit cell size (high S_S) can accelerate material degradation. Beyond the S_S of the macrostructure, the degradation rate of scaffolds can also be regulated through several independent approaches, such as the modification of surface roughness [64] and the introduction of inherent micropores [71] within struts. These methods effectively increase surface area at microscopic scales.

Lattice-driven, nature-inspired, and biomimetic porous materials have attracted notable attention because of their intriguing geometric connections and attractive physical properties [12, 72–74]. However, the properties of porous biomaterials, such as elastic modulus, permeability, yield strength, manufacturability, anisotropic design, and gradient design, have already been investigated. In our opinion, the next step in the microdesign of bone repair implants is the elucidation of interactions between bone and tissue regeneration, such as tissue differentiation and remodeling, as well as the investigation of cellular and tissue responses to quantifiable mechanical stimuli.

4 Limitations

Herein, uniform-thickness bone regeneration was employed as a proxy for temporal progression, which might deviate from actual bone regeneration. While prior studies [15, 25, 59] have demonstrated significant effects of local geometry on cell adhesion, cell migration, and tissue regeneration, this study focused primarily on the long-term effects of geometric parameters (pore size, surface area) rather than on simulating realistic bone regeneration. Consequently, this approximation does not compromise the validity of our conclusions. Additionally, the findings obtained herein are applicable to the bone–implant interfaces in artificial joints or large-segment bone defects. Smaller bone scaffolds facilitate rapid full-volume bone regeneration and do not require deep bone ingrowth. Finally, 400 μm was assumed as the lower limit for pore size, as this assumption was validated from both permeability and mechanobiological perspectives. Although pores smaller than 400 μm can still facilitate osseointegration [17], such pores are typically employed for surface bone regeneration (e.g., coatings) and are not designed for long-term, deep bone ingrowth.

5 Conclusions

Herein, we simulated the dynamic interactions between the pore size/surface area of bone implants and generated bone tissue across multiple temporal scales, using precisely partitioned spatial volumes. The samples with a high specific surface area (S_S) facilitated the rapid formation of new bone tissue during the early implantation stage. However, their smaller pores tended to cause occlusions, hindering further tissue development. In contrast, although low-S_S samples exhibited slower bone regeneration, their larger pores were found to provide adequate physical space for tissue regeneration and mass transport, ultimately promoting bone formation in the long term. From a mechanobiological perspective, as time progresses (and tissue thickness increases), the mechanical environment of the newly formed tissue tends to promote the formation of fibrous tissue, thereby inhibiting the generation of additional bone mass. This suggests that the mechanical environment maintains a trade-off between bone regeneration and pore size, ensuring adequate space for mass transport over the long term.

Acknowledgements We appreciate the financial support from the National Natural Science Foundation of China (No. 52035012) and the Guangdong Basic and Applied Basic Research Foundation (No. 2025A1515012203).

Author contributions XP: conceptualization, methodology, software, and writing—original draft. GXZ: methodology and software. JP: methodology, writing—original draft, and resources. SY: methodology. WC: methodology. XZ: methodology and writing—review & editing. SXQ: methodology and supervision. ZMJ: resources, writing—review & editing, and supervision.

Declarations

Conflict of interest The authors declare that they have no known competing financial interests or personal relationships that could have appeared to influence the work reported in this paper.

Ethical approval This study does not contain any studies with human or animal subjects performed by any of the authors.

Data availability The data used to support the findings of this study are available from the corresponding authors upon request.

Use of generative AI tools During the preparation of this work, the authors used DeepSeek to improve language and readability. After using this tool, the authors reviewed and edited the content as needed and take full responsibility for the content of the publication.

References

1. Peng X, Huo Y, Zhang GX et al (2023) Controlled mechanical and mass-transport properties of porous scaffolds through hollow strut. *Int J Mech Sci* 248:108202. https://doi.org/10.1016/j.ijmecsci.2023.108202
2. Zadpoor AA (2019) Meta-biomaterials. *Biomater Sci* 8(1): 18–38. https://doi.org/10.1039/c9bm01247h
3. Meisterhans M, Dimitriou D, Fasser MR et al (2024) Influence of offset on osseointegration in cementless total hip arthroplasty: a finite element study. *J Orthop Res* 42(7):1566–1576.

https://doi.org/10.1002/jor.25808
4. Page RS, Pai V, Eng K et al (2018) Cementless versus cemented glenoid components in conventional total shoulder joint arthroplasty: analysis from the Australian Orthopaedic Association National Joint Replacement Registry. *J Shoulder Elb Surg* 27(10):1859–1865. https://doi.org/10.1016/j.jse.2018.03.017
5. Luger M, Holzbauer M, Klotz MC et al (2024) Cementless short stem total hip arthroplasty in patients older than 75 years: is it feasible? *Arch Orthop Trauma Surg* 144(8):3715–3727. https://doi.org/10.1007/s00402-024-05425-z
6. Zhang LF, Ge SR, Liu HT et al (2015) Contact damage failure analyses of fretting wear behavior of the metal stem titanium alloy–bone cement interface. *J Mech Behav Biomed Mater* 51: 132–146. https://doi.org/10.1016/j.jmbbm.2015.06.025
7. Campana V, Milano G, Pagano E et al (2014) Bone substitutes in orthopaedic surgery: from basic science to clinical practice. *J Mater Sci Mater Med* 25(10):2445–2461. https://doi.org/10.1007/s10856-014-5240-2
8. Wallace IJ, Worthington S, Felson DT et al (2017) Knee osteoarthritis has doubled in prevalence since the mid-20th century. *Proc Natl Acad Sci USA* 114(35):9332–9336. https://doi.org/10.1073/pnas.1703856114
9. Yuan L, Ding SL, Wen CE (2019) Additive manufacturing technology for porous metal implant applications and triple minimal surface structures: a review. *Bioact Mater* 4:56–70. https://doi.org/10.1016/j.bioactmat.2018.12.003
10. Feng JW, Fu JZ, Yao XH et al (2022) Triply periodic minimal surface (TPMS) porous structures: from multi-scale design, precise additive manufacturing to multidisciplinary applications. *Int J Extreme Manuf* 4(2):022001. https://doi.org/10.1088/2631-7990/ac5be6
11. Gupta A, Talha M (2015) Recent development in modeling and analysis of functionally graded materials and structures. *Prog Aerosp Sci* 79:1–14. https://doi.org/10.1016/j.paerosci.2015.07.001
12. Liang YJ, He HY, Yin J et al (2024) Dynamic compressive behavior of functionally graded triply periodic minimal surface cellular structures. *Eng Struct* 312:118260. https://doi.org/10.1016/j.engstruct.2024.118260
13. Chen JQ, Song CH, Deng ZT et al (2024) Functional gradient design of additive manufactured gyroid tantalum porous structures: manufacturing, mechanical behaviors and permeability. *J Manuf Process* 125:202–216. https://doi.org/10.1016/j.jmapro.2024.07.054
14. Alemayehu DB, Todoh M, Huang SJ (2025) Hybrid biomechanical design of dental implants: integrating solid and gyroid triply periodic minimal surface lattice architectures for optimized stress distribution. *J Funct Biomater* 16(2):54. https://doi.org/10.3390/jfb16020054
15. Wang Y, Liu Y, Chen SS et al (2025) Enhancing bone regeneration through 3D printed biphasic calcium phosphate scaffolds featuring graded pore sizes. *Bioact Mater* 46:21–36. https://doi.org/10.1016/j.bioactmat.2024.11.024
16. Ye F, Yang H, Hong CH et al (2025) Design and characterization of 3D printed gradient scaffolds with spatial distribution of pore sizes. *Ceram Int* 51(9):12185–12196. https://doi.org/10.1016/j.ceramint.2025.01.070
17. Chang B, Song W, Han TX et al (2016) Influence of pore size of porous titanium fabricated by vacuum diffusion bonding of titanium meshes on cell penetration and bone ingrowth. *Acta Biomater* 33:311–321. https://doi.org/10.1016/j.actbio.2016.01.022
18. Zhao Y, Wu QQ, Zhao CW et al (2024) Progress of structural scaffold biomaterials for bone tissue defect repair: a cutting-edge review. *Compos Struct* 349:118542. https://doi.org/10.1016/j.compstruct.2024.118542
19. Foroughi AH, Valeri C, Razavi MJ (2025) A review of computational optimization of bone scaffold architecture: methods, challenges, and perspectives. *Prog Biomed Eng* 7(1):012003. https://doi.org/10.1088/2516-1091/ad879a
20. Ouyang PR, Dong H, He XJ et al (2019) Hydromechanical mechanism behind the effect of pore size of porous titanium scaffolds on osteoblast response and bone ingrowth. *Mater Des* 183:108151. https://doi.org/10.1016/j.matdes.2019.108151
21. Kolken HMA, Callens SJP, Leeflang MA et al (2022) Merging strut-based and minimal surface meta-biomaterials: decoupling surface area from mechanical properties. *Addit Manuf* 52: 102684. https://doi.org/10.1016/j.addma.2022.102684
22. Peng X, Li SY, He DY et al (2024) Expanding the mechanical and mass-transport combination for bone scaffolds: through stretched structure. *Compos Struct* 329:117783. https://doi.org/10.1016/j.compstruct.2023.117783
23. Sun CN, Dong EC, Chen JY et al (2022) The promotion of mechanical properties by bone ingrowth in additive-manufactured titanium scaffolds. *J Funct Biomater* 13(3):127. https://doi.org/10.3390/jfb13030127
24. Peng X, He DY, Shen TT et al (2025) Gaussian curvature-mechanical environment-tissue regeneration relationships at the bone-implant interface of porous implants: a simulation study. *Med Eng Phys* 142:104343. https://doi.org/10.1016/j.medengphy.2025.104343
25. Yang YH, Xu TP, Bei HP et al (2022) Gaussian curvature-driven direction of cell fate toward osteogenesis with triply periodic minimal surface scaffolds. *Proc Natl Acad Sci USA* 119(41): e2206684119. https://doi.org/10.1073/pnas.2206684119
26. Zhi W, Wang XH, Sun D et al (2022) Optimal regenerative repair of large segmental bone defect in a goat model with osteoinductive calcium phosphate bioceramic implants. *Bioact Mater* 11:240–253. https://doi.org/10.1016/j.bioactmat.2021.09.024
27. Pobloth AM, Checa S, Razi H et al (2018) Mechanobiologically optimized 3D titanium-mesh scaffolds enhance bone regeneration in critical segmental defects in sheep. *Sci Transl Med* 10(423):eaam8828. https://doi.org/10.1126/scitranslmed.aam8828
28. Peng X, Huang QY, Zhang YL et al (2021) Elastic response of anisotropic Gyroid cellular structures under compression: parametric analysis. *Mater Des* 205:109706. https://doi.org/10.1016/j.matdes.2021.109706
29. Yang L, Yan CZ, Fan HY et al (2019) Investigation on the orientation dependence of elastic response in Gyroid cellular structures. *J Mech Behav Biomed Mater* 90:73–85. https://doi.org/10.1016/j.jmbbm.2018.09.042
30. Ma S, Tang Q, Han XX et al (2020) Manufacturability, mechanical properties, mass-transport properties and biocompatibility of triply periodic minimal surface (TPMS) porous scaffolds fabricated by selective laser melting. *Mater Des* 195:109034. https://doi.org/10.1016/j.matdes.2020.109034
31. Lu T, Sun ZW, Jia CW et al (2023) Roles of irregularity of pore morphology in osteogenesis of Voronoi scaffolds: from the perspectives of MSC adhesion and mechano-regulated osteoblast differentiation. *J Biomech* 151:111542. https://doi.org/10.1016/j.jbiomech.2023.111542
32. Perier-Metz C, Cipitria A, Hutmacher DW et al (2022) An in silico model predicts the impact of scaffold design in large bone

defect regeneration. *Acta Biomater* 145:329–341. https://doi.org/10.1016/j.actbio.2022.04.008
33. Poltue T, Karuna C, Khrueaduangkham S et al (2021) Design exploration of 3D-printed triply periodic minimal surface scaffolds for bone implants. *Int J Mech Sci* 211:106762. https://doi.org/10.1016/j.ijmecsci.2021.106762
34. Shum JM, Gadomski BC, Tredinnick SJ et al (2023) Enhanced bone formation in locally-optimised, low-stiffness additive manufactured titanium implants: an *in silico* and *in vivo* tibial advancement study. *Acta Biomater* 156:202–213. https://doi.org/10.1016/j.actbio.2022.04.006
35. Yánez A, Cuadrado A, Martel O et al (2018) Gyroid porous titanium structures: a versatile solution to be used as scaffolds in bone defect reconstruction. *Mater Des* 140:21–29. https://doi.org/10.1016/j.matdes.2017.11.050
36. Song FC, Wang LL, Zhang YH et al (2025) Design of an ultra-low modulus 3D printed titanium bio-metamaterials for bone replacement. *Addit Manuf Front* 4(1):200197. https://doi.org/10.1016/j.amf.2025.200197
37. Montazerian H, Davoodi E, Asadi-Eydivand M et al (2017) Porous scaffold internal architecture design based on minimal surfaces: a compromise between permeability and elastic properties. *Mater Des* 126:98–114. https://doi.org/10.1016/j.matdes.2017.04.009
38. Huo Y, Lu Y, Meng L et al (2021) A critical review on the design, manufacturing and assessment of the bone scaffold for large bone defects. *Front Bioeng Biotechnol* 9:753715. https://doi.org/10.3389/fbioe.2021.753715
39. Reimeringer M, Nuño N (2016) The influence of contact ratio and its location on the primary stability of cementless total hip arthroplasty: a finite element analysis. *J Biomech* 49(7): 1064–1070. https://doi.org/10.1016/j.jbiomech.2016.02.031
40. Minku, Mukherjee K, Ghosh R (2024) Assessment of bone ingrowth around beaded coated tibial implant for total ankle replacement using mechanoregulatory algorithm. *Comput Biol Med* 175:108551. https://doi.org/10.1016/j.compbiomed.2024.108551
41. Liu X, Niebur GL (2008) Bone ingrowth into a porous coated implant predicted by a mechano-regulatory tissue differentiation algorithm. *Biomech Model Mechanobiol* 7(4):335–344. https://doi.org/10.1007/s10237-007-0100-3
42. Ghosh R, Chanda S, Chakraborty D (2020) The influence of macro-textural designs over implant surface on bone on-growth: a computational mechanobiology based study. *Comput Biol Med* 124:103937. https://doi.org/10.1016/j.compbiomed.2020.103937
43. Claes LE, Heigele CA (1999) Magnitudes of local stress and strain along bony surfaces predict the course and type of fracture healing. *J Biomech* 32(3):255–266. https://doi.org/10.1016/S0021-9290(98)00153-5
44. Yang L, Han CJ, Wu HZ et al (2020) Insights into unit cell size effect on mechanical responses and energy absorption capability of titanium graded porous structures manufactured by laser powder bed fusion. *J Mech Behav Biomed Mater* 109:103843. https://doi.org/10.1016/j.jmbbm.2020.103843
45. Peng X, Huang QY, Zhang GX et al (2022) Compensating the anisotropic mechanical properties of electron beam melting-based Gyroid scaffolds using structural design. *Int J Mech Sci* 226:107442. https://doi.org/10.1016/j.ijmecsci.2022.107442
46. Revilla-León M, Ceballos L, Martínez-Klemm I et al (2018) Discrepancy of complete-arch titanium frameworks manufactured using selective laser melting and electron beam melting additive manufacturing technologies. *J Prosthet Dent* 120(6): 942–947. https://doi.org/10.1016/j.prosdent.2018.02.010
47. Yang E, Leary M, Lozanovski B et al (2019) Effect of geometry on the mechanical properties of Ti-6Al-4V Gyroid structures fabricated via SLM: a numerical study. *Mater Des* 184:108165. https://doi.org/10.1016/j.matdes.2019.108165
48. Ochoa I, Sanz-Herrera JA, García-Aznar JM et al (2009) Permeability evaluation of 45S5 Bioglass®-based scaffolds for bone tissue engineering. *J Biomech* 42(3):257–260. https://doi.org/10.1016/j.jbiomech.2008.10.030
49. Foroughi AH, Razavi MJ (2022) Multi-objective shape optimization of bone scaffolds: enhancement of mechanical properties and permeability. *Acta Biomater* 146:317–340. https://doi.org/10.1016/j.actbio.2022.04.051
50. Truscello S, Kerckhofs G, Van Bael S et al (2012) Prediction of permeability of regular scaffolds for skeletal tissue engineering: a combined computational and experimental study. *Acta Biomater* 8(4):1648–1658. https://doi.org/10.1016/j.actbio.2011.12.021
51. Zhao Y, Wu QQ, Wu LZ (2025) Mass transport characteristic and biocompatibility of demand-guided structural biomaterials. *Compos Struct* 355:118848. https://doi.org/10.1016/j.compstruct.2025.118848
52. Cheong VS, Fromme P, Mumith A et al (2018) Novel adaptive finite element algorithms to predict bone ingrowth in additive manufactured porous implants. *J Mech Behav Biomed Mater* 87: 230–239. https://doi.org/10.1016/j.jmbbm.2018.07.019
53. Lu YT, Cui ZT, Cheng LL et al (2020) Quantifying the discrepancies in the geometric and mechanical properties of the theoretically designed and additively manufactured scaffolds. *J Mech Behav Biomed Mater* 112:104080. https://doi.org/10.1016/j.jmbbm.2020.104080
54. Song X, Li H, Li R et al (2018) Osteogenesis effect of dynamic mechanical loading on MC3T3-E1 cells in three-dimensional printing biomimetic composite scaffolds. *Chin J Reparat Reconstruct Surg* 32(4):448–456 (in Chinese). https://doi.org/10.7507/1002-1892.201711091
55. Meinert C, Schrobback K, Hutmacher DW et al (2017) A novel bioreactor system for biaxial mechanical loading enhances the properties of tissue-engineered human cartilage. *Sci Rep* 7(1): 16997. https://doi.org/10.1038/s41598-017-16523-x
56. Brockstedt H, Bollerslev J, Melsen F et al (1996) Cortical bone remodeling in autosomal dominant osteopetrosis: a study of two different phenotypes. *Bone* 18(1):67–72. https://doi.org/10.1016/8756-3282(95)00424-6
57. Wang Y, Wang L, Soro N et al (2024) Bone ingrowth simulation within the hexanoid, a novel scaffold design. *3D Print Addit Manuf* 11(6):1949–1960. https://doi.org/10.1089/3dp.2023.0113
58. Taniguchi N, Fujibayashi S, Takemoto M et al (2016) Effect of pore size on bone ingrowth into porous titanium implants fabricated by additive manufacturing: an *in vivo* experiment. *Mater Sci Eng C* 59:690–701. https://doi.org/10.1016/j.msec.2015.10.069
59. Liang HX, Chao L, Xie DQ et al (2022) Trabecular-like Ti–6Al–4V scaffold for bone repair: a diversified mechanical stimulation environment for bone regeneration. *Compos Part B Eng* 241:110057. https://doi.org/10.1016/j.compositesb.2022.110057
60. Klein-Nulend J, Bakker AD, Bacabac RG et al (2013) Mechanosensation and transduction in osteocytes. *Bone* 54(2):182–190. https://doi.org/10.1016/j.bone.2012.10.013
61. Liu YJ, Wang L, Zhang J et al (2025) A design strategy for

long-term stability of porous PEEK implants by regulation of porous structure and in vivo mechanical stimulation. *Bio-Des Manuf* 8(2):275–287. https://doi.org/10.1631/bdm.2400259
62. Sun CN, Kang JF, Wang L et al (2023) Stress-dependent design and optimization methodology of gradient porous implant and application in femoral stem. *Comput Meth Biomech Biomed Eng* 26(11):1308–1319. https://doi.org/10.1080/10255842.2022.2115291
63. Naghavi SA, Tamaddon M, Garcia-Souto P et al (2023) A novel hybrid design and modelling of a customised graded Ti-6Al-4V porous hip implant to reduce stress-shielding: an experimental and numerical analysis. *Front Bioeng Biotechnol* 11:1092361. https://doi.org/10.3389/fbioe.2023.1092361
64. Qin Y, Wen P, Guo H et al (2019) Additive manufacturing of biodegradable metals: current research status and future perspectives. *Acta Biomater* 98:3–22. https://doi.org/10.1016/j.actbio.2019.04.046
65. Moravej M, Mantovani D (2011) Biodegradable metals for cardiovascular stent application: interests and new opportunities. *Int J Mol Sci* 12(7):4250–4270. https://doi.org/10.3390/ijms12074250
66. Chen HM, Shi Q, Shui HT et al (2021) Degradation of 3D-printed porous polylactic acid scaffolds under mechanical stimulus. *Front Bioeng Biotechnol* 9:691834. https://doi.org/10.3389/fbioe.2021.691834
67. Yazdimamaghani M, Razavi M, Vashaee D et al (2017) Porous magnesium-based scaffolds for tissue engineering. *Mater Sci Eng C* 71:1253–1266. https://doi.org/10.1016/j.msec.2016.11.027
68. Wen P, Jauer L, Voshage M et al (2018) Densification behavior of pure Zn metal parts produced by selective laser melting for manufacturing biodegradable implants. *J Mater Process Technol* 258:128–137. https://doi.org/10.1016/j.jmatprotec.2018.03.007
69. Li S, Yang HT, Qu XH et al (2024) Multiscale architecture design of 3D printed biodegradable Zn-based porous scaffolds for immunomodulatory osteogenesis. *Nat Commun* 15(1):3131. https://doi.org/10.1038/s41467-024-47189-5
70. Nie Y, Chen G, Peng HB et al (2021) *In vitro* and 48 weeks *in vivo* performances of 3D printed porous Fe-30Mn biodegradable scaffolds. *Acta Biomater* 121:724–740. https://doi.org/10.1016/j.actbio.2020.12.028
71. Xie DX, Zhou QN, He YL et al (2025) 3D printed metal structures with inherent micro pores to enhance biodegradability and absorbability. *Addit Manuf* 109:104837. https://doi.org/10.1016/j.addma.2025.104837
72. Zadpoor AA, Hedayati R (2016) Analytical relationships for prediction of the mechanical properties of additively manufactured porous biomaterials. *J Biomed Mater Res Part A* 104(12): 3164–3174. https://doi.org/10.1002/jbm.a.35855
73. Zhang Q, Gong H, Shi PP et al (2025) Design and mechanical properties of a 3D missing rib structure inspired by crystal twinning. *Mater Today Commun* 43:111786. https://doi.org/10.1016/j.mtcomm.2025.111786
74. Liu H, Chen H, Sun B et al (2025) Enhancing angiogenesis and osseointegration through a double gyroid Ti6Al4V scaffold with triply periodic minimal surface. *Bio-Des Manuf* 8(1):36–54. https://doi.org/10.1631/bdm.2400114